POLITECNICO DI TORINO
Repository ISTITUZIONALE

Experimental base flow modification on a swept wing using plasma forcing

Availability:
This version is available at: 11583/2976879 since: 2023-03-14T07:04:27Z

Terms of use:

(Article begins on next page)

17 October 2023

Experimental base flow modification on a swept wing using plasma forcing F

K. Peng (彭开晟), J. P. W. Arkesteijn, F. Avallone, et al.

COLLECTIONS

F This paper was selected as Featured

View Online   Export Citation   CrossMark
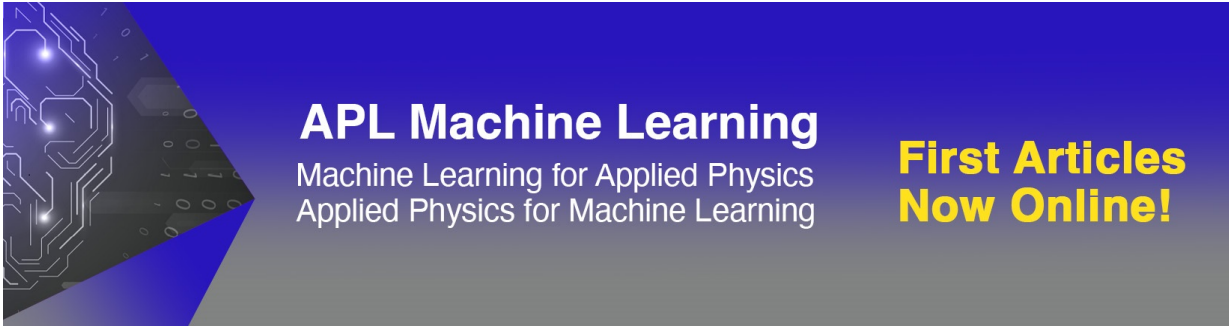
ARTICLES YOU MAY BE INTERESTED IN

Unsteady disturbances in a swept wing boundary layer due to plasma forcing
Physics of Fluids **34**, 114115 (2022); https://doi.org/10.1063/5.0124818

Transition due to isolated roughness in a swept wing boundary layer
Physics of Fluids **34**, 084113 (2022); https://doi.org/10.1063/5.0101187

On finite amplitude solitary waves—A review and new experimental data
Physics of Fluids **34**, 101304 (2022); https://doi.org/10.1063/5.0109902

Experimental base flow modification on a swept wing using plasma forcing Ⓕ

View Online   Export Citation   CrossMark

K. Peng (彭开晟),[a)] [iD] J. P. W. Arkesteijn, [iD] F. Avallone, [iD] and M. Kotsonis [iD]

AFFILIATIONS

FPT Department, Faculty of Aerospace Engineering, Delft University of Technology, Kluyverweg 1, 2629HS Delft, The Netherlands

[a)]Author to whom correspondence should be addressed: K.Peng@tudelft.nl

ABSTRACT

This work experimentally investigates plasma actuator (PA) forcing effects on the base flow and developing crossflow (CF) instabilities in a swept wing boundary layer. Spanwise-invariant plasma forcing near the leading edge is configured according to the base flow modification (BFM) strategy. A simplified predictive model is constructed by coupling an experimentally derived plasma body force and a linear stability theory and is used to infer the stability characteristics of the boundary layer subject to BFM. The base flow velocity is measured by stereo particle image velocimetry (PIV) at various PA operating conditions. Similarly, the developing CF instabilities, triggered through discrete roughness elements, are quantified by planar-PIV. The results demonstrate that a PA can reduce the boundary layer CF component, whereas the control authority shows a high dependence on the momentum coefficient. The dissimilar reduction between the streamline-aligned velocity and CF component leads to a local re-orientation of the base flow. Spanwise spectral analysis of the time-averaged flow indicates that stationary CF instabilities can be favorably manipulated whereas the BFM reduction effects depend on the corresponding initial amplitudes of stationary instabilities. An evident spanwise shift in the trajectory of stationary CF vortices is observed, which appears to result from the local alteration of the boundary layer stability due to the PA forcing. Despite the overall reduction in the amplitude of stationary CF instabilities, unsteady disturbances are found to be enhanced by the PA forcing. The current results shed light on the underlying principles of BFM-based PA operation in the context of laminar flow control.

I. INTRODUCTION

Swept wings are inherent to many modern transport aircraft. The flow over a swept wing is characterized by a three-dimensional boundary layer where the so-called crossflow (CF) component emerges in a direction locally normal to the external inviscid streamline. This secondary flow features an inflection point and provides a source for the CF instabilities, which ultimately dominate the laminar–turbulent transition.[1] Among primary modes of CF instabilities, traveling modes prevail and dominate the boundary layer in conditions of high free-stream turbulence intensity T_u. In contrast, in realistic cruise flight conditions (i.e., low T_u), the swept wing boundary layer is dominated by stationary CF instabilities, which are mainly triggered and affected by the surface roughness, particularly near the leading edge. Specifically, the strong velocity shear generated by the stationary modes provokes unsteady secondary instabilities, which grow rapidly and eventually lead to transition. Extensive reviews on this topic are summarized by Saric et al.,[1] Bippes,[2] and Malik et al.[3]

Over recent decades, considerable research has been devoted to the formation and developing mechanisms of CF instabilities with an ultimate aim of controlling these instabilities, thus delaying the impending transition. Laminar flow control (LFC) has been established as an umbrella term encompassing a variety of passive and active strategies for transition delay in both two- and three-dimensional boundary layers. Within LFC, surface suction has played a pivotal role. In three-dimensional boundary layers, slot-panel or hole-panel suction systems were demonstrated to reduce the CF component, resulting in significant transition delay. Related experiments and flight campaigns on this topic are described by Joslin,[4] Krishnan et al.,[5] and Messing and Kloker.[6] Nevertheless, the complexity, weight, and cost of these suction-based techniques pose challenges in applicability and robustness, highlighting the need for simpler control alternatives.

Recognizing these challenges, Saric et al.[7] proposed a fully passive approach, where equispaced discrete roughness elements (DREs) were placed on swept wings in the vicinity of a leading edge. Following the same concept, the more generalized term upstream flow deformation (UFD) was proposed by Wassermann and Kloker[8] and refer to all capable devices/techniques operating on the principle of sub-critical

mode excitation. In brief, the DRE/UFD technique leverages the non-linear interaction between artificially triggered sub-critical stationary modes and naturally growing critical stationary modes, leading to the stabilization of the latter. However, despite extensive verification by several wind tunnel studies,[1,9] successful transition delay by DRE/UFD could not be consistently confirmed in recent flight tests.[10] The challenge of successfully applying DRE/UFD has been attributed to, among others, a high sensitivity of this method to external factors such as DRE quality, residual roughness, and freestream turbulence intensity.[11] Additionally, a purely passive approach can be less effective or even detrimental in off-design or changing conditions, which exposes the need for active (or reactive) control methods.

Within the active flow control techniques, interest in plasma-based actuators (PAs) emerged in recent decades due to their particular features such as low power consumption, fast response, and fully electronic operation without moving parts.[12,13] Based on the principle of gas ionization, the PA generates a volume-distributed body force, which leads to a localized flow acceleration. Working mechanisms and characterization of PA are summarized by Kotsonis,[13] Corke et al.,[14] and Benard and Moreau.[15] Addressing LFC, the majority of PA-based flow control applications focus on two-dimensional boundary layers[16–18] while attempts in three-dimensional boundary layers began more recently. The relative ease of implementation of PA (both numerically and experimentally) has led to the formulation of several strategies aimed at swept wing transition control. These encompass mainly upstream flow deformation (UFD), direct attenuation, and base flow modification (BFM). The plasma-based UFD strategy essentially follows the concept of the aforementioned DRE/UFD approach, where the PA works as tunable roughness to amplify sub-critical stationary modes, which non-linearly interact and damp critical stationary modes. In contrast, the direct attenuation strategy places the PA at selected spanwise positions to directly (i.e., linearly) oppose and weaken the rotation of stationary CF vortices. Both plasma-based UFD and direct attenuation strategies have been extensively evaluated in numerical studies.[19–24] However, due to the strict requirements for

PA geometry and position required by these two strategies, only limited experimental studies are reported.[25–28]

Different from these two strategies, the BFM strategy is theoretically independent from the nature of incoming instabilities and ambient conditions, as it aims at directly reducing the source of CF instabilities, namely, the CF component in the boundary layer. Through BFM, the base flow can be stabilized, and growth rates of both stationary and traveling CF instabilities are reduced, eventually yielding transition delay. In the most straightforward implementation of BFM, a linear and spanwise-invariant PA is placed near the leading edge and oriented to directly counteract the CF component [as shown in Fig. 1(a)]. However, it should be noted that the discrete, spanwise-modulated PA configurations adopted in the aforementioned UFD and direct attenuation strategies have been found to perform a local BFM action as well.[11] By doing this, the discrete PA needs to be carefully placed in relation to the incoming CF instabilities to avoid triggering unwanted stationary CF vortices.[20]

In the early numerical work on plasma-based BFM by Dörr and Kloker,[20] the PA was modeled as a steady (i.e., time invariant) body force, inserted as a source term in the Navier–Stokes (NS) equations. The results demonstrated the importance of 2D mean flow distortion in stabilizing the boundary layer. Based on these numerical predictions, Serpieri et al.[27] fabricated and applied a 2D straight (i.e., spanwise-invariant) PA on a swept wing model and found that low-frequency velocity fluctuations were amplified even when the PA operated at high forcing frequency f_{AC}. A simplified body force model was proposed and indicated that these unsteady disturbances could be related to the stochastic dynamics of PA electrical discharge. This assumption was further experimentally confirmed by Moralev et al.[29] and attributed to the quasi-stochastic nature of PA micro-discharge formation. By using even higher f_{AC} than Serpieri et al.,[27] the work of Yadala et al.[30] demonstrated, for the first time experimentally, successful BFM transition delay by a 2D straight PA. In the same work, the amplitude reduction of CF instabilities was predicted by a simplified numerical model employing an experimentally determined body force
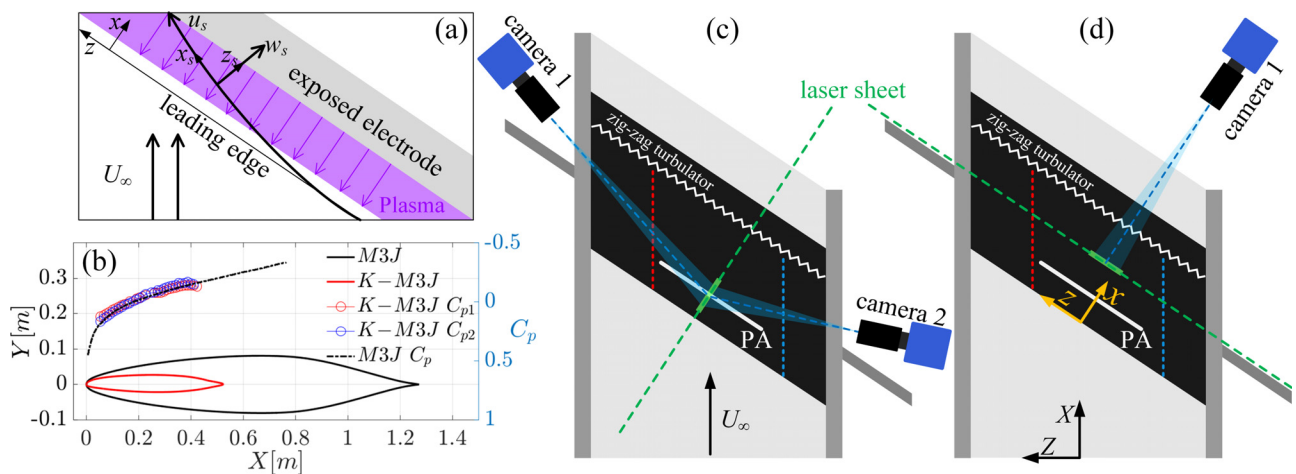
FIG. 1. (a) Schematic of BFM-based PA forcing (not to-scale). Note that the streamline-aligned $x_s y_s z_s$ system is right-handed; (b) wing cross section (in the X direction) and experimental pressure coefficient C_p of M3J and $K-M3J$. C_{p1} and C_{p2} refer to the upper and lower pressure taps of $K-M3J$, located along the red and blue dashed lines, respectively, in (c); (c) schematic of the stereo-PIV arrangement; (d) schematic of the planar-PIV arrangement.

(as proposed by Serpieri et al.[27]). Similarly, Baranov et al.[31] placed a so-called multi-discharge actuator (MDA) at a downstream location where stationary modes attained the maximum growth rate. The results demonstrated the reduction of the CF component as well as amplitudes of critical stationary CF instabilities while no evident sub-critical modes were induced. Yadala et al.[25] compared BFM and UFD strategies by estimating the movement of transition location and the net power gain from drag reduction. The results indicated that, compared with UFD, BFM appeared to be more robust but less effective due to the higher input power.

Though the BFM strategy was experimentally demonstrated to delay transition,[30] the direct effect of an operating PA on the CF component of a swept wing boundary layer has yet to be characterized experimentally. More importantly, the relation between PA operating parameters and the eventual attenuation of CF component needs to be established in order to fully elucidate the working principle of this method. Furthermore, low-frequency disturbances can possibly be induced by PA forcing, as a result of the inherent micro-discharge formations of plasmas.[29] As a consequence, traveling CF instabilities could be parasitically induced by the PA due to their relatively larger growth rate in respect to stationary modes. Therefore, a boundary layer manipulated by a BFM-based PA is expected to be dominated by both stationary and traveling CF instabilities, which necessitates the elucidation of PA's effects on both types. In this work, a BFM-tailored PA is experimentally investigated on a scaled swept wing model. The achieved CF reduction and the base flow direction are traced under various momentum coefficient c_μ, which, in turn, is controlled by the applied high voltage amplitude V_{p-p}. Moreover, the streamwise growth of stationary and unsteady CF instabilities is investigated with respect to the PA action.

This paper is organized as follows: In Section II, the experimental setup and PA parameters are described as well as the linear stability theory estimation for the baseline case. The experimental results of base flow modification and the CF reduction are presented in Sec. III. Section IV reports the PA effects on the development of both stationary and unsteady CF instabilities. Finally, the conclusions of this study are summarized in Sec. V.

II. EXPERIMENTAL SETUP AND METHODOLOGY
A. Swept wing model and wind tunnel facility

The present experiment is conducted in the anechoic vertical tunnel (A-tunnel) at Delft University of Technology, featuring a sufficiently low turbulence intensity ($T_u < 0.1\%$) for the development of stationary CF instabilities.[32] The swept wing model $K - M3J$ is used in this experiment, which is purposely designed to replicate the near-leading edge pressure coefficient C_p of the frequently used reference model $66018M3J$.[33] The small leading edge radius and the favorable C_p gradient of $K - M3J$ guarantee the dominance of CF instabilities in the boundary layer, while avoiding the attachment line and Tollmien–Schlichting instabilities. In addition, the $K - M3J$ model features a sweep angle of $45°$ and a wide recessed groove of 3.1 mm thickness, which is purposely designed for the flush mounting of the PA assembly. The complete design and performance of the $K - M3J$ model are detailed by Peng and Kotsonis.[34] In this study, the flow over the swept wing's pressure side was investigated. The wing cross section (in the X direction) and corresponding experimental pressure coefficient C_p, measured through two streamwise rows of surface mounted

pressure taps, are given in Fig. 1(b). The C_p is measured at angle of attack $\alpha = 3.5°$ and at freestream velocity $U_\infty = 22$ m/s ($Re_X = 7.72 \times 10^5$, based on the swept chord $c_X = 523.3$ mm, where c_X is along the X direction). Zig-zag turbulators are placed at $x/c_x = 0.8$ on the pressure side and $x/c_x = 0.2$ on the suction side to trip the boundary layer in order to avoid flow separation at the trailing edge. Three coordinate reference systems are used, namely, the wind tunnel-aligned XYZ, wing-aligned curvilinear xyz, and streamline-aligned $x_s y_s z_s$, as shown in Fig. 1. It should be noted that Y is normal to the XZ plane. In contrast, the xyz system is body-fitted with x and y being locally tangent and normal to the airfoil surface, respectively, while z is parallel to the leading edge. The corresponding velocity vectors are denoted as $[U\ V\ W]$, $[u\ v\ w]$, and $[u_s\ v_s\ w_s]$. Specifically, x_s is tangential to the local inviscid streamline (z_s is normal to the inviscid streamline), as illustrated in Fig. 1(a).

For the entirety of this work, overbar symbols denote non-dimensional quantities. For the base flow measurements (Sec. III), the velocity components are non-dimensionalized by the total freestream velocity U_∞, while for the instability characterization (Sec. IV), velocity components are non-dimensionalized by the spanwise freestream velocity component w_∞. Additionally, y is non-dimensionalized as $\bar{y} = y/\delta_0$, where δ_0 is the Blasius length scale. $\delta_0 = \nu s_0/u_0 = 1.77 \times 10^{-4}$ m is used as the reference length, where $u_0 = 12.13$ m/s is the boundary layer edge velocity at $x/c_x = 0.0594$. Specifically, ν is the kinematic viscosity while $s_0 = 0.0251$ m is the surface distance from the leading edge to $x/c_x = 0.0594$.

Two particle image velocimetry (PIV) arrangements are used to quantify the flow field, namely, stereoscopic PIV returning three velocity components $[u\ v\ w]$ for the base flow characterization and planar-PIV returning two velocity components $[v\ w]$ for the investigation of CF instabilities. In the stereo-PIV arrangement, the flow field is measured with the laser sheet oriented in the xy plane. (The z position of the measurement plane is fixed at the PA mid-span.) Two LaVision Imager cameras (sCMOS, 2560×2160 pixels) are placed on each side of the test section with a suitable stereoscopic aperture angle, acquiring at a sampling frequency of 13 Hz. A schematic of the stereo-PIV setup is displayed in Fig. 1(c). The flow field is constructed as the ensemble average of 500 instantaneous stereo-PIV vector fields. For the planar-PIV arrangement, an automated traversing system shifts the laser and camera units together, thus maintaining their alignment. The schematic of the planar-PIV setup is displayed in Fig. 1(d). The laser sheet is aligned in the yz plane at $x/c_x = 0.125$, and the measurements are taken at several chordwise locations from $x/c_x = 0.125$ to 0.3 with an interval of 0.025. Due to the minimal curvature of the wing model in this domain, the measurement planes are approximately normal to the local wall tangent at all locations. The data are acquired at a sampling frequency of 13 Hz, and time-averaged and standard deviation fields are extracted from 1000 instantaneous vector fields per case. Given the low temporal resolution (compared to the flow dynamics) of both PIV measurements, the time-averaged velocity and standard deviation fields acquired by both stereo-PIV and planar-PIV are uncorrelated.

It should be noted that, due to the laser light reflection and the high velocity uncertainty near the wall, velocity information in these regions is deemed not sufficiently reliable and discarded from further analysis. Namely, data at $y < 0.1$ mm are not considered for the stereo-PIV results while data at $y < 0.2$ mm are cropped for the planar-PIV results. The time-average uncertainty[35] is calculated for

both stereo-PIV and planar-PIV in the boundary layer and the free-stream, respectively. For the stereo-PIV, the maximum statistical uncertainty in the boundary layer is estimated as 0.24%U_∞ for the u component and 0.87%U_∞ for the w component. In the freestream, the average uncertainty is estimated as 0.017%U_∞ for u and 0.047%U_∞ for w. For planar-PIV, the maximum uncertainty for the w component is identified as 0.22%U_∞ in the boundary layer while the average uncertainty in the freestream is 0.029%U_∞.

B. Plasma actuator and discrete roughness elements

In swept wing flows, the external inviscid-streamline is almost aligned with the z axis in the vicinity of the leading edge. Therefore, PA forcing in the direction of the x axis can be expected to also counteract the CF component w_s, as shown in Fig. 1(a). Following the same approach used by Yadala et al.,[30] a 2D straight dielectric barrier discharge (DBD) PA is placed parallel to the leading edge with the interface between exposed and encapsulated electrodes located at $x/c_x = 0.073$. It should be noted that the exposed electrode is connected to the high voltage, and the encapsulated electrode is connected to the ground. The spanwise invariance of the actuator mitigates the possible introduction of unwanted spanwise modulation of the flow. The encapsulated electrode is placed upstream of the exposed electrode with no gap between each other. The PA electrodes are fabricated using automatic inkjet printing of silver conductive paint, featuring a width of 5 mm and a spanwise extent of 160 mm. The model groove designed for PA is filled with a composite layer of polyethylene terephthalate (PET) foils of various thicknesses on which the PA is printed. Due to the sensitivity of CF instabilities to the surface roughness, the PET foil (i.e., dielectric material) is wrapped around the leading edge and extends downstream to avoid any surface irregularity. A Trek 20/20C HS amplifier is chosen as the power supply for PA, through which the sinusoidal high voltage signal is generated and delivered to the actuator.[27]

The collisional process between ionized species and neutral air particles is generally responsible for the momentum transfer between the plasma discharge and the fluid. Therefore, the macroscopic effect of the PA can be regarded as a volume-distributed body force applied on the fluid.[15]

The flow field in the vicinity of an operating PA is acquired in a separate PIV experiment, which acquires at a sampling frequency of 20 kHz, as reported by Arkesteijn.[36] Using the reduced method by Kotsonis et al.,[37] the body force distribution of the used PA is calculated for various peak-to-peak voltage V_{p-p} based on quiescent flow

measurements enabled through planar-PIV measurements. It should be noted that the present study only measured the body force at quiescent conditions since the magnitude and general force distribution are assumed largely independent of external velocities for the investigated conditions based on the estimates by Pereira et al.[38] In addition, for the entirety of this work, the PA is operated at a fixed carrier frequency $f_{AC} = 5$ kHz. The x-aligned body force component F_x in quiescent conditions is illustrated in Fig. 2(a) for $V_{p-p} = 14$ kV. To visually compare the spatial topology of the body force distribution with the characteristic scale of the experimentally-measured boundary layers, several CF component profiles w_s/u_{se} and the boundary layer thickness δ_{99} (where $u = 99\%u_\infty$, u_∞ is the local freestream component u at the boundary layer edge) are extracted from the stereo-PIV measurements for the reference case ($U_\infty = 22$ m/s, PA-off). Specifically, u_{se} is the local streamline-aligned velocity at the boundary layer edge. As shown in Fig. 2(a), the employed body force extends almost throughout the boundary layer. Although at different forcing amplitudes, the general topology appears similar to the most efficient forcing configuration found by Dörr and Kloker.[20] That is, the most effective PA forcing is attained when the volume force distribution covers almost the complete boundary layer but does not extend beyond the boundary layer edge. For various flow conditions pertaining to this study and PA operating parameters, the actuation momentum coefficient is calculated as[30]

$$c_\mu = \frac{\iint_s F_x ds}{\frac{1}{2}\rho u_e^2 \theta_u},\qquad(1)$$

where u_e is the local edge velocity in the x axis direction (at $x/c_x = 0.073$) and θ_u is the local boundary layer momentum thickness based on u. The dependence of c_μ on V_{p-p} and U_∞ is illustrated in Fig. 2(b). For the remainder of this work, various momentum coefficients c_μ are used (Table I) and serve as a measure of the relative PA forcing strength.

As mentioned earlier, stationary CF instabilities dominate transition at realistic cruise flight conditions. To clarify the effect of the BFM strategy, the existence and development of stationary CF instabilities are required conditions for this experiment. In this study, DRE arrays featuring a spacing of $\lambda = 8$ mm are placed at $x/c_x = 0.02$ to promote critical stationary CF vortices (i.e., most amplified mode according to the linear stability theory, as described in Sec. II C) of different amplitudes. The height and diameter of the used DRE arrays have
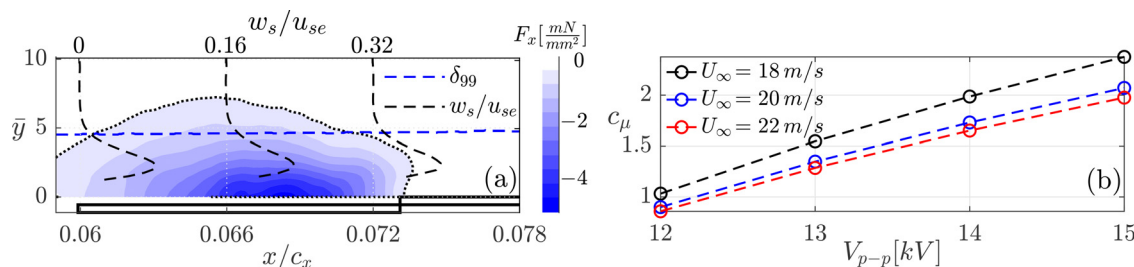
FIG. 2. (a) Experimentally measured body force distribution F_x at $V_{p-p} = 14$ kV. The dotted line denotes $F_{x,10\%} = 10\% F_{x,max}$. Black dashed lines illustrate the spanwise-averaged profiles of w_s/u_{se} for the reference case at $x/c_x = 0.06$, 0.066, and 0.072 (abscissa-shifted by 0.16). Blue dashed line refers to the unforced boundary layer thickness δ_{99}; (b) PA momentum coefficient c_μ corresponding to various input voltage amplitude V_{p-p}.

TABLE I. PA momentum coefficient c_μ at various V_{p-p} and U_∞.

U_∞	18 m/s	20 m/s	22 m/s
$V_{p-p} = 12$ kV	$c_\mu = 1.03$	$c_\mu = 0.9$	$c_\mu = 0.86$
$V_{p-p} = 15$ kV	$c_\mu = 2.38$	$c_\mu = 2.07$	$c_\mu = 1.98$

been characterized using a precision laser profilometer. Specifically, the DRE-L array features an element height of $h_{DRE} = 0.1147$ ± 0.0023 mm, and the DRE-H array features $h_{DRE} = 0.2179$ ± 0.0031 mm, both of which have a diameter of $d_{DRE} = 1.772$ ± 0.017 mm.[39]

C. Estimations of BFM efficacy based on the linear stability theory

As mentioned in the Introduction, the PA can potentially induce perturbations at undesired frequencies, which in turn enhance unsteady CF instabilities and other types of boundary layer instabilities, even at low T_u conditions, thus potentially affecting the BFM efficacy.[25] Nevertheless, since the BFM strategy is designed to directly reduce the CF component (i.e., the driver of CF instabilities), both stationary and traveling CF instabilities are expected to be suppressed. To preliminarily assess the described effects, a simplified PA forcing model is employed as proposed by Serpieri et al.[27] The experimental pressure distribution and measured velocity profiles u and w at $x/c_x = 0.0551$ ($U_\infty = 22$ m/s) are used as top and inflow boundary conditions for this model, in which the time-invariant, incompressible Navier–Stokes equations are numerically solved, using the finite element multiphysics tool COMSOL. The experimentally determined body force ($c_\mu = 1.65$) is set as a steady source term in the NS momentum equations [as shown in Fig. 3(a)] and is adjusted to qualitatively match the experimentally measured boundary layer velocity when the PA is active (i.e., PA-on). As shown in Fig. 3(b), the simulated shape factor H_{12} qualitatively matches the experimental case, especially for PA-off. The simulation also captures the abrupt increase

in the shape factor due to the flow-opposing plasma forcing (i.e., local blockage) while no flow separation is observed in either numerical or experimental fields. The streamline-aligned velocity u_s and CF velocity w_s are calculated and subtracted from the PA-off case (e.g., $\Delta \bar{u}_s = \bar{u}_{s,\text{on}} - \bar{u}_{s,\text{off}}$, where the subscripts on and off indicate the PA state). The velocity profiles u_s/u_{se} and w_s/u_{se} are compared at several streamwise locations ($x/c_x = 0.08, 0.09, 0.1, 0.11,$ and 0.12) and displayed by dashed lines for PA-off and solid lines for PA-on, respectively. Consistent with the results of Yadala et al.,[30] u_s and w_s are found to be reduced by the BFM-based PA forcing, providing a first confirmation of the principle mechanism of the BFM strategy.

To further assess the BFM effects on the boundary layer stability, the linear stability theory (LST) is employed. Based on the numerically calculated boundary layer, the Orr–Sommerfeld equation is solved in spatial formulation with various combinations of angular frequency ω ($= 2\pi f s_0/u_0$) and spanwise wavenumber β ($= 2\pi s_0/\lambda$). A full theoretical description of LST is described by Mack,[40] while the numerical implementation is similar to the one used by Rius-Vidales and Kotsonis.[41]

The non-dimensional growth rate $-\bar{\alpha}_i = -\alpha_i \delta_0$ and N factor are calculated for various frequencies and spanwise wavelengths, as shown in Fig. 4. The N factors are illustrated by the iso-lines, where dashed lines refer to PA-off. The change in the growth rate is calculated as $\Delta \bar{\alpha}_i = -\bar{\alpha}_{i,\text{on}} - (-\bar{\alpha}_{i,\text{off}})$ and indicated by the colored contours. As shown in the PA-off case in Fig. 4(a), the stationary CF modes appear to be most integrally amplified at a wavelength of approximately $\lambda = 8$ mm in the domain of interest. This result demonstrates the analogy of $K - M3J$'s boundary layer to that of $M3J$ used in previous works.[27,30] Within the concerned domain and for the entirety of this work, the $\lambda = 8$ mm mode is taken as the critical stationary mode. Regarding the traveling CF instabilities, the N factor attains a maximum for modes at approximately $f = 200$ Hz and rapidly decreases when f further increases.

As expected, the reduced CF component due to PA forcing results in the reduced growth rate for both stationary and traveling CF instabilities. However, compared with stationary CF instabilities, the
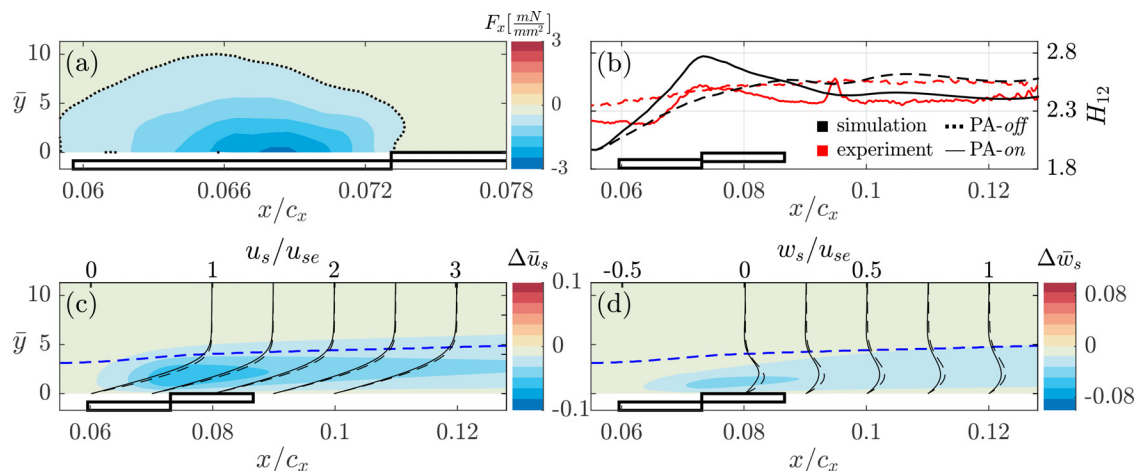
FIG. 3. (a) Experimentally determined body force; (b) shape factor H_{12}; (c) contours of streamline-aligned velocity reduction $\Delta \bar{u}_s$ due to plasma forcing; (d) contours of CF velocity reduction $\Delta \bar{w}_s$. Blue dashed line in (c) and (d) indicates the boundary layer thickness δ_{99} (PA-off). Velocity profiles u_s/u_{se} and w_s/u_{se} are illustrated at $x/c_x = 0.08$, 0.09, 0.1, 0.11, and 0.12, where corresponding u_s/u_{se} is abscissa-shifted by 0.5 and w_s/u_{se} by 0.25. PA operating at $c_\mu = 1.65$ and $U_\infty = 22$ m/s.
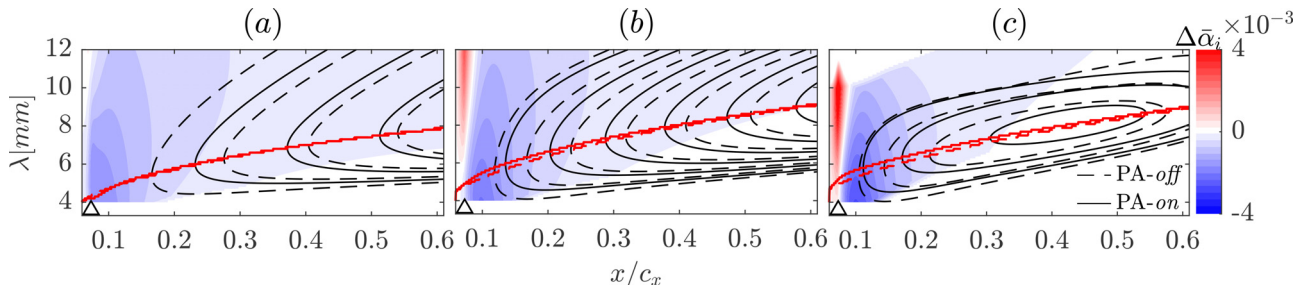
FIG. 4. Change in the amplification rate $\Delta\bar{\alpha}_i$ (colored) and N factor (iso-lines) due to plasma forcing at $c_\mu = 1.65$ for (a) stationary CF instabilities; (b) traveling CF instabilities at $f = 200$ Hz; (c) traveling CF instabilities at $f = 400$ Hz. The N iso-lines increase from 1 with an interval of 0.5. Additionally, the dashed iso-lines refer to PA-off, and solid iso-lines refer to PA-on. The triangle indicates the PA location while red lines indicate λ of the mode attaining the locally maximum N factor.

stabilizing effect appears to be more evident on traveling CF instabilities. This effect is consistent with the observations of Dörr and Kloker,[20] which were attributed to the larger influence of 2D mean flow deformation on traveling CF modes. Furthermore, the BFM effect is more evident for modes of smaller λ as a significant reduction is observed in both stationary and traveling CF instabilities especially in the upstream portion of the considered domain. Additionally, the maximum N factor is traced in the streamwise direction, and the corresponding λ is illustrated by the red lines (dashed lines refer to PA-off). The result evidently demonstrates that the forcing exerts a selective effect on the λ of the most amplified modes. Specifically, the traveling modes appear more susceptible to this effect as λ of the most amplified mode noticeably becomes larger.

## III. PA EFFECTS ON THE BASE FLOW

In this section, the attained base flow modification by the PA action is described, followed by an evaluation of amplitudes of streamline-aligned flow components (i.e., u_s and w_s) and the direction of the base flow. The flow field is constructed as a time-averaged ensemble of the stereo PIV vector fields, through which the three-dimensional velocity vector ($u\,v\,w$) is recorded. The PIV results are

shown in the body-fitted xy plane. It must be emphasized that the base flow experiment and following analysis in this section are performed on a clean wing, namely, without DRE. This was chosen to ensure a largely spanwise invariant development of the boundary layer, which is essentially devoid of any stationary or traveling CF vortices due to the low residual roughness on the surface as well as minimal free-stream turbulence in the wind tunnel. The velocity components u and w are later used to calculate the streamline-aligned velocity u_s and the corresponding CF component w_s. The velocity transformation from the wing-attached reference system to the streamline reference system is applied as[42]

$$\begin{pmatrix} u_s \\ w_s \end{pmatrix} = \begin{pmatrix} \cos\phi_s(x) & \sin\phi_s(x) \\ \cos\phi_s(x) & -\sin\phi_s(x) \end{pmatrix} \begin{pmatrix} u \\ w \end{pmatrix},$$

where $\phi_s(x)$ is the local angle between the inviscid external streamline and the x axis and defined as $\phi_s(x) = \tan^{-1}(w_\infty(x)/u_\infty(x))$, where $u_\infty(x)$ and $w_\infty(x)$ are the local freestream velocity components (in the direction of x and z, respectively).

Figure 5 illustrates two representative cases ($c_\mu = 2.38$ and $c_\mu = 1.98$) where the relative changes of velocities $\Delta\bar{u}_s = u_{s,\text{on}} - u_{s,\text{off}}$
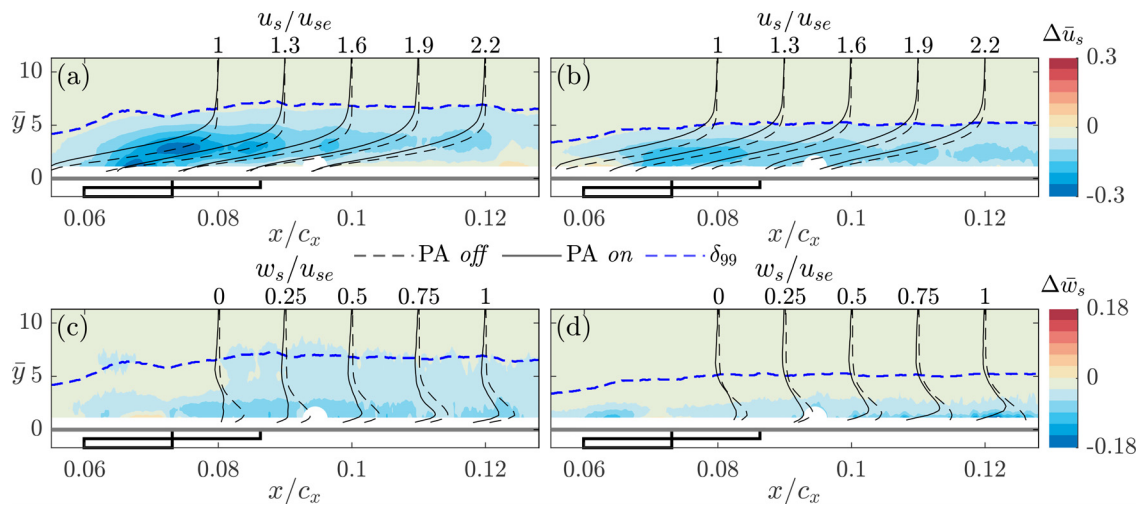
FIG. 5. Velocity reduction $\Delta\bar{u}_s$ and $\Delta\bar{w}_s$ for (a) and (c) $c_\mu = 2.38$; (b) and (d) $c_\mu = 1.98$. Blue dashed line indicates the boundary layer thickness δ_{99} for PA-on. Velocity profiles of u_s/u_{se} and w_s/u_{se} are shown at $x/c = 0.08, 0.09, 0.1, 0.11,$ and 0.12. The velocity profiles u_s/u_{se} are abscissa-shifted by 0.3 and w_s/u_{se} by 0.25.

and $\Delta\bar{w}_s = w_{s,\text{on}} - w_{s,\text{off}}$ are calculated. The velocity profiles u_s/u_{se} and w_s/u_{se} are compared at chordwise locations from $x/c_x = 0.08$ to 0.12 with a step of 0.01. The data in the white circle around $x/c_x = 0.094$ are discarded due to the laser light reflection. Nevertheless, the present results demonstrate that the PA effect on the base flow is mainly limited inside the boundary layer. As shown in Fig. 5(a), u_s is significantly reduced by the PA action for both low and high c_μ cases. A region of decelerated flow is found above the encapsulated electrode where the body force is typically centralized [i.e., the region of plasma discharge, Fig. 2(a)]. The decelerating effect also imposes a direct influence on the boundary layer thickness δ_{99}, which is locally increased. On the other hand, the velocity profiles of u_s/u_{se} become less full under the PA forcing, indicating that du_s/dy (a measure of the skin friction coefficient) is reduced in the vicinity of PA. This result, however, is not contradictory to the observation of Dörr and Kloker,[20] where u_s and skin friction are found amplified since the corresponding PA forcing is applied in z and z_s directions.

As expected, the velocity reduction effect shows a strong dependence on c_μ as the PA loses control authority on the boundary layer when c_μ is reduced in agreement with Yadala *et al.*[25,30] A similar trend is found in Fig. 5(b), where the CF component w_s experiences a notable reduction due to PA forcing. The evident decrease in the maximum CF component, which develops in the vicinity of the centralized body force, agrees well with the numerical predictions of Dörr and Kloker.[20] On the other hand, the present results illustrate that the PA imparts momentum along both x_s and z_s directions, as expected from the working mechanism of the BFM method. Nonetheless, the larger reduction values found of u_s demonstrate that the PA imparts more momentum against u_s, in the present case. This highlights the important role of BFM forcing orientation with respect to the local CF component. Considering the inviscid streamline inclination, for a 2D straight actuator, moving the actuator close to the attachment line can maximize the BFM effects. However, moving the PA close to the attachment line should take the PA strength (i.e., c_μ) into consideration to avoid possible boundary layer separation.

To further quantify the PA influence on the base flow, non-dimensional momentum integrals along y, namely, $\bar{M}_{us}$ and $\bar{M}_{ws}$ (based on u_s and w_s) are calculated at each chord location x/c_x as follows:

$$\begin{aligned} \bar{M}_{us} &= \frac{1}{\delta_{99}} \int_0^{\delta_{99}} |\rho\bar{u}_s|\bar{u}_s \, dy, \\ \bar{M}_{ws} &= \frac{1}{\delta_{99}} \int_0^{\delta_{99}} |\rho\bar{w}_s|\bar{w}_s \, dy, \end{aligned} \quad (2)$$

where ρ is the constant flow density. The ratio $\bar{M}_{\text{on}}/\bar{M}_{\text{off}}$ is calculated as a measure of the boundary layer momentum change due to PA

forcing. The momentum integral change $\bar{M}_{\text{on}}/\bar{M}_{\text{off}}$ at various c_μ is displayed in Fig. 6. The outcomes demonstrate a general momentum loss in u_s within the boundary layer. The PA ability in reducing $\bar{M}_{us}$ appears as a strong function of c_μ where the larger c_μ benefits the PA authority on the base flow modification. In cases of higher c_μ, the $\bar{M}_{us}$ undergoes an evident decrease above the ground electrode where the body force is localized. Moreover, the decrease in $\bar{M}_{us}$ appears to remain downstream in the measuring domain. Nonetheless, the streamline-aligned component u_s of the boundary layer is comprised of the majority of flow momentum. As such, the relative PA effects on the u_s momentum are minimal as the maximum decrease in the ratio $\bar{M}_{us,\text{on}}/\bar{M}_{us,\text{off}}$ is only around 2%. In contrast, a significant effect of the PA forcing is observed on the considerably weaker CF component w_s. A significant reduction of $\bar{M}_{ws,\text{on}}/\bar{M}_{ws,\text{off}}$ is found above the encapsulated electrode, indicating the strong local effect of PA. At the condition of higher c_μ, the ratio $\bar{M}_{ws,\text{on}}/\bar{M}_{ws,\text{off}}$ even becomes negative above the encapsulated electrode, indicating that the momentum of the CF component undergoes a local inversion due to the forcing. In spite of the lower absolute reduction in w_s found in Fig. 5, the present results demonstrate that the relative change of w_s is more significant due to the weaker CF component. It can be concluded that the BFM strategy modifies the base flow mainly by modifying the target w_s.

Due to the dissimilar effects of BFM on u_s and w_s, the local direction of the PA-affected boundary layer is expected to deviate from the natural (i.e., unforced) trajectory and shift toward the external freestream line. To confirm this assumption, the base flow angle is quantified by the following equation:

$$\phi(y/\delta_{99}) = \tan^{-1}(\bar{w}(y/\delta_{99})/\bar{u}(y/\delta_{99})). \quad (3)$$

The relative angle change $\Delta\phi = \phi_{\text{on}} - \phi_{\text{off}}$ is calculated for various c_μ and illustrated in Fig. 7. The results are calculated at several wall-normal locations, namely, $y/\delta_{99} = 0.3$, 0.5, 0.7, and 3, referring to conditions inside and outside the boundary layer, respectively. The results inside the boundary layer ($y/\delta_{99} = 0.3$, 0.5, and 0.7) evidently demonstrate the re-orientation of the boundary layer flow due to the PA forcing. Specifically, the angle change $\Delta\phi$ appears to be determined by both y/δ_{99} and c_μ, where lower y/δ_{99} and larger c_μ lead to a larger alteration. In agreement with the behavior of $\bar{M}_{ws,\text{on}}/\bar{M}_{ws,\text{off}}$ observed in Fig. 6(b), a similar trend is found for the base flow angle change $\Delta\phi$. Initially, the base flow is locally deviated by the PA forcing and further recovers until the PA interface, after which $\Delta\phi$ increases again and remains downstream. For cases of higher c_μ, the base flow is even inverted toward the opposite direction. On the other hand, the flow outside the boundary layer ($y/\delta_{99} = 3$) appears to be minimally influenced [Fig. 7(d)]. Small deviations within $\pm 0.5°$ are nevertheless
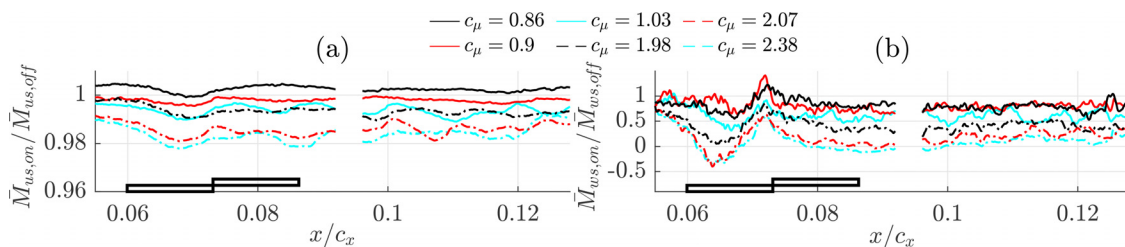

FIG. 6. Momentum integral modification due to PA forcing of (a) $\bar{M}_{us,\text{on}}/\bar{M}_{us,\text{off}}$ and (b) $\bar{M}_{ws,\text{on}}/\bar{M}_{ws,\text{off}}$.
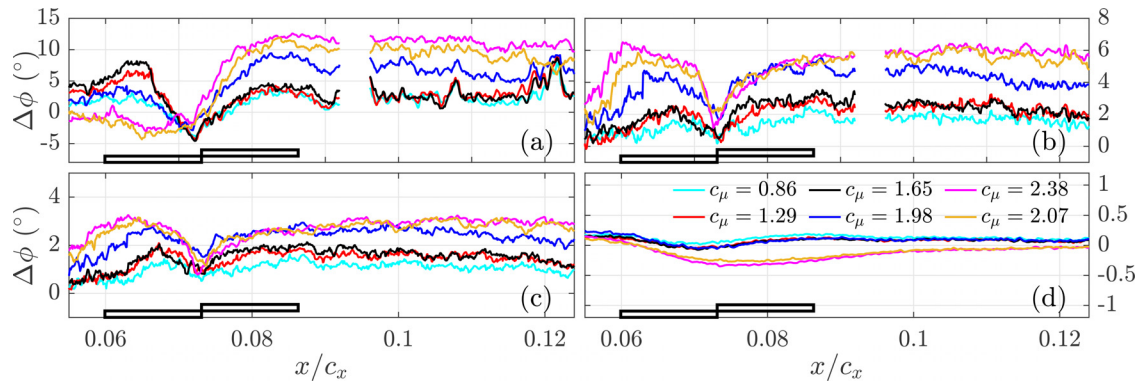
FIG. 7. Base flow angle change $\Delta\phi$ for various c_μ at (a) $y/\delta_{99} = 0.3$; (b) $y/\delta_{99} = 0.5$; (c) $y/\delta_{99} = 0.7$; (d) $y/\delta_{99} = 3$.

observed, which are expected to diminish further away from the wing surface.

A simple schematic is given in Fig. 8 to conceptualize the above process. As demonstrated in Fig. 8(a), inside the boundary layer ($y/\delta_{99} < 1$), the flow direction is determined by the vector components u_s and w_s while determined only by u_s outside the boundary layer ($y/\delta_{99} > 1$). Figure 8(b) illustrates how the PA forcing modifies the base flow trajectory within the boundary layer. At unforced flow conditions (PA-off), the base flow will be slightly offset from the free-stream line due to the existence of w_s. When the PA is on, the free-stream remains unchanged due to the limited PA effect outside the boundary layer. However, the base flow undergoes a considerable distortion due to the significant reduction of w_s. As a result, the modified base flow vectors are directed toward the freestream direction.

The results of this section generally follow observations of Wassermann and Kloker[8] and Dörr and Kloker.[20] In their numerical simulations, a two-dimensional mean-flow distortion is induced by hole-array suction or distributed PA forcing, respectively, generally followed by a diminishing CF component. The resulting distortion significantly suppresses the growth of critical stationary CF instabilities and becomes a decisive factor for stabilizing the boundary layer. Recalling the previously observed w_s reduction and identified base flow shift, the present results experimentally confirm the ability of BFM-based PA forcing to impose a similar two-dimensional distortion on the current base flow.

IV. PA EFFECTS ON CROSSFLOW INSTABILITIES

In this section, the streamwise evolution of stationary and unsteady CF instabilities is investigated under PA forcing. During the

experimental investigation, the PA is operated at a fixed set of parameters ($V_{p-p} = 14$ kV, $U_\infty = 22$ m/s, $c_\mu = 1.65$). Two DRE cases of different forcing amplitudes are investigated, primarily aimed at introducing stationary CF vortices of low (DRE-L) or high (DRE-H) amplitude, respectively. The motivation in varying the initial amplitude of the stationary CF modes is to examine the influence of the BFM effect on linearly (i.e., low amplitude) and non-linearly growing (i.e., high amplitude) CF modes.

A. Effect on stationary structures

The time-averaged velocity $\bar{w}$ at $x/c_x = 0.225$ for the representative case DRE-H is illustrated in Fig. 9(a), revealing uniform stationary vortices appearing at the spacing dictated by the forcing DRE. Similar observation is found in the DRE-L case (not shown here for brevity), albeit the stationary vortices appear significantly weaker. In addition, to investigate the PA effects on the discrete stationary modes, the spanwise periodicity of the mean flow $\bar{w}$ is leveraged, through a spatial Fast Fourier Transform (FFT) of the velocity field [Fig. 9(a)] at constant $\bar{y}$. Spectral amplitudes $\bar{A} = A_{FFT}/w_\infty$ for both DRE-L and DRE-H cases are given in Fig. 10, illustrated from $x/c_x = 0.125$ to 0.3. The black dashed lines indicate the non-dimensional wavenumber $\bar{k}$ of 0.5, 1, and 2 ($\bar{k} = 1/\bar{\lambda}$, $\bar{\lambda} = \lambda/\lambda_{DRE}$), corresponding to λ of 16, 8, and 4 mm, respectively. Hereafter, the stationary mode featuring $\lambda_{DRE} = 8$ mm refers to the fundamental mode (i.e., $\bar{k} = \bar{\lambda} = 1$). The spectral results generally confirm the dominance of the fundamental mode in the boundary layer, for both DRE-L and DRE-H cases. As shown in Fig. 10(a), DRE-L effectively forces the fundamental mode
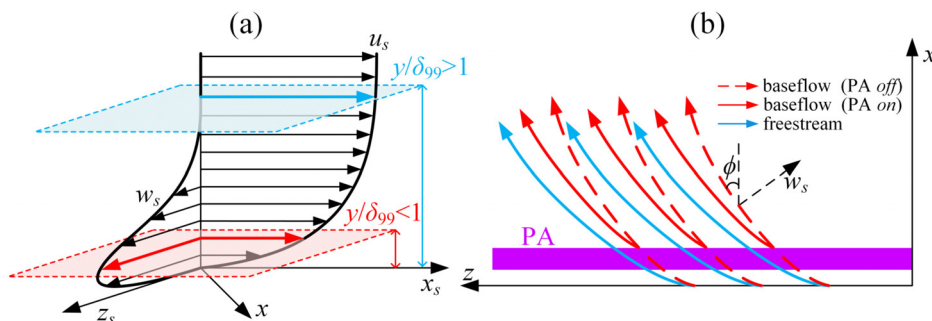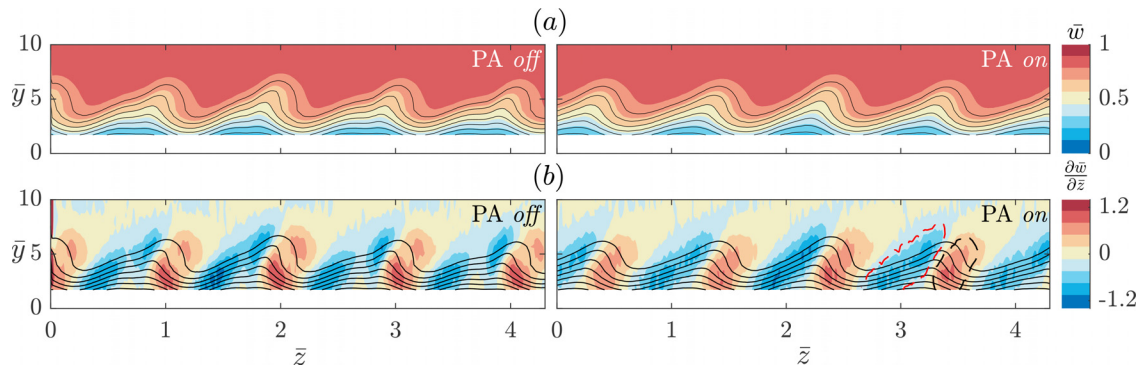

FIG. 8. Schematic of (a) swept wing boundary layer profiles and corresponding velocity vectors in the *xz* plane; (b) trajectories of the boundary layer flow and freestream line.

FIG. 9. (a) Time-averaged velocity fields $\bar{w}$ and (b) spanwise gradient of mean flow $\partial\bar{w}/\partial\bar{z}$ for the DRE-*H* case. Plane location is at $x/c_x = 0.225$, and black iso-lines illustrate $\bar{w}$, ten levels from 0 to 0.9. The regions outlined by dashed lines in (b) are based on thresholds of -0.23 and 0.5.

for PA-off where evident peaks are found in the spectra. Moreover, high energy peaks are also found at the super-harmonic mode $\bar{k} = 2$ while no distinct sub-harmonic can be identified. When PA is on, the fundamental mode and super-harmonics are evidently weakened by the PA forcing. This result coincides with the general expectations of the BFM technique, as predicted by the simplified model [Fig. 4(a)]. In spite of the attenuation of discrete spectral peaks (at the super-harmonic modes) due to PA forcing, evident disturbances are found amplified in a broad range of $\bar{k} < 1$. While no conclusive reasoning can be provided on the origin of these long-wavelength disturbances, several possible factors can be proposed. Among others, these can include possible slow variance or modulation of plasma discharge strength along the spanwise direction due to misalignments in actuator fabrication and placement. A dedicated sensitivity study to such parameters would be important to elucidate this effect, however it falls beyond the scope of the present work.

Based on the observed weakening of stationary CF modes due to PA forcing, secondary effects can be expected on other important features such as the velocity gradients. Figure 9(b) illustrates the spanwise gradient of the time-averaged velocity $\partial\bar{w}/\partial\bar{z}$. Inside the core of the stationary CF vortices, two distinct regions are identified where

$\partial\bar{w}/\partial\bar{z}$ obtains a local minimum and maximum, respectively [regions outlined by dashed lines in Fig. 9(b)]. Particularly in cases of strongly amplified stationary CF vortices, early theoretical and numerical work has identified the minimum spanwise gradient region to be related to the emergence of type I secondary instability while the maximum spanwise gradient region to be associated with the type III primary traveling instability.[3,8] For PA-off, two local peaks are observed in both minimum and maximum gradient regions, which results from the emergence of the harmonic mode of $\lambda = 4$ mm. In contrast, the gradient regions become more continuous and centralized for PA-on, signaling that the PA forcing has an inhibitory effect on the harmonic mode, which is confirmed by the spectral analysis (Fig. 10). Additionally, the PA forcing noticeably reduces the maximum gradient amplitudes, indicating that the shear stress (modulated by stationary CF vortices) is weakened by the PA forcing. As noted earlier, the spanwise shear modification in the flow can be expected to have an influence on the development of traveling CF instabilities and other unsteady disturbances. Dedicated discussion on these effects is provided in Sec. IV C.

To further quantify the PA effects on the evolution of the fundamental mode and its harmonics, the corresponding Fourier modes are
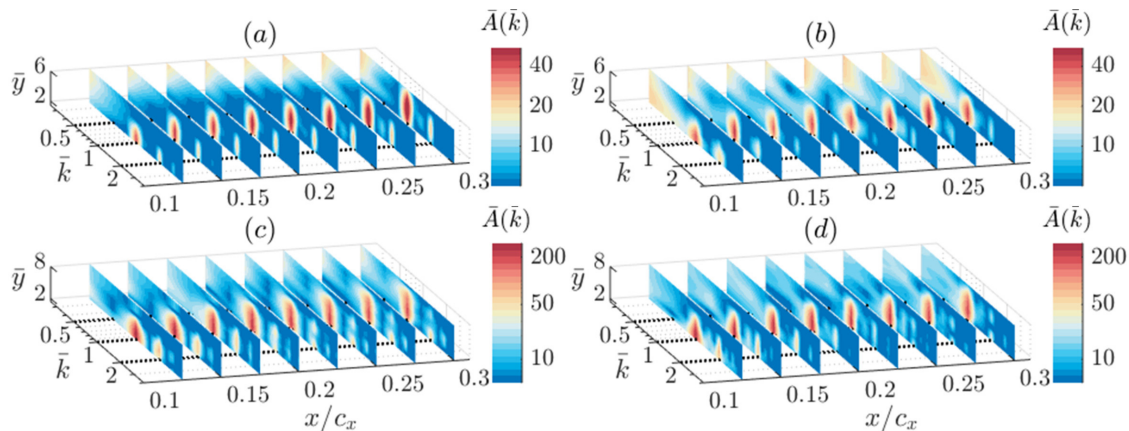
FIG. 10. Non-dimensional spectral amplitude $\bar{A}(\bar{k})$ for (a) DRE-*L*, PA-off; (b) DRE-*L*, PA-on; (c) DRE-*H*, PA-off; (d) DRE-*H*, PA-on. Spectral planes are plotted from $x/c_x = 0.125$ to 0.3 with a step of 0.025. Wavenumbers $\bar{k}$ of 0.5, 1, and 2 correspond to wavelengths λ of 16, 8, and 4 mm (black dashed lines). The colorbar follows a logarithmic scale.

reconstructed through the inverse Fourier transform. The maximum standard deviation of the reconstructed velocity profiles is calculated as the amplitude of the interested stationary mode. The quantity is denoted as $\langle \bar{w}(\bar{k}) \rangle_{\max}$ and the corresponding location is denoted as $\bar{y}_{\max}$. Figure 11 illustrates the modal amplitudes pertaining to the two DRE cases with selected Fourier modes of $\bar{k} = 0.5$, 1, 2, and 4 (corresponding to $\lambda = 16, 8, 4, 2$ mm). Specifically, in the DRE-*L* case, the cyan line in Fig. 11(a) illustrates amplitudes of the fundamental mode estimated by LST at PA-off, artificially scaled to match with the experimental amplitude of PA-off at $x/c_x = 0.3$. The blue line illustrates the LST amplitudes of PA-on and matches with the LST amplitude of PA-off at the starting point ($x/c_x = 0.0594$).

Evidently, the experimental growth rate of the fundamental mode agrees well with the LST prediction, confirming the linearity of the DRE-*L* case. For PA-on, the fundamental mode amplitudes qualitatively match with the LST prediction. A significant reduction of the fundamental mode (approximately 32.1% at $x/c_x = 0.25$) is found in experimental results, demonstrating the stabilizing effect of the BFM technique. Similarly, the PA forcing effectively reduces the super-harmonic mode $\bar{k} = 2$ while having no evident effect on the sub-harmonic mode $\bar{k} = 0.5$. The amplitude reduction of the super-harmonic stationary modes can be attributed to several combined effects. First, as the fundamental mode is suppressed, the resulting non-linear growth of higher-order harmonics can be expected to be delayed. Second, as originally hypothesized for the BFM technique, the suppression of the CF component in the plasma region stabilizes the boundary layer for CF modes of all wavelengths, including the $\bar{k} = 2$ mode.

Figure 11(b) illustrates the modal amplitudes for the DRE-*H* case. As expected from the relatively higher h_{DRE}, the fundamental mode in the imaged domain features significantly larger amplitudes compared with DRE-*L*. In addition, the fundamental mode is not growing and even mildly decays downstream, no longer agreeing with the LST prediction. This signifies a possible non-linear amplitude saturation, which is reached upstream of the measurement domain. In combination to the development of the characteristic secondary lobe of CF vortices evident in Fig. 9(a), this behavior indicates the non-linear stage of stationary CF instabilities for the DRE-*H* case. Considering the PA forcing, compared with DRE-*L*, the fundamental mode in the DRE-*H* case appears almost unaffected by the BFM effect. On the other hand, the super-harmonic modes $\bar{k} = 2$ and $\bar{k} = 4$ are

significantly weakened by the PA forcing, similar to the observations in DRE-*L*. This outcome can be attributed to the specific DRE amplitude (i.e., h_{DRE}), which in turn conditions the strength of stationary CF vortices arriving at the PA forcing region. Specifically, the inability of BFM to impart noticeable changes on the fundamental mode within the measurement domain can be related to the already high amplitude of the latter as they reach the plasma forcing region. In addition, even if there would be a local amplitude decrease due to BFM, the saturation of the fundamental mode upstream of the observed domain would prevent it from growing further in both PA-on and PA-off cases. In contrast, it appears that the super-harmonic modes are more susceptible to the BFM authority, which reconciles well with the LST results where N factors are more effectively reduced for sub-critical stationary modes in the considered domain [Fig. 4(a), $x/c_x = 0.125$ to 0.3]. These observations suggest that the BFM's effects can show a dependence to the wavelengths of incoming stationary CF instabilities. If so, the wavelength of the instabilities arriving at the PA location can be a deciding factor for the success of BFM method, in addition to the expected influence of the momentum coefficient (i.e., relative forcing strength). Further parametric variations of forced mode wavelengths are deemed necessary in the future work in order to clarify this point.

B. Effect on stationary structure trajectory

In addition to modifying amplitudes of stationary structures, the BFM strategy shows an evident effect on the stationary CF vortices' trajectories. During the experiment, the PA forcing was found to produce a notable spanwise shift of stationary CF vortices along the z axis in both DRE cases, as already demonstrated by the DRE-*H* case in Fig. 9(a). Specifically, while the CF vortices remain topologically similar between PA-on and PA-off cases, they are evidently shifted toward $+z$; thus, the wavenumber vector is forced toward the x axis. This shift has also been observed in previous experimental and numerical studies and related to the local PA-based BFM effects.[20,31] It can be hypothesized that the spanwise shift of stationary CF vortices is coupled to the previously observed re-orientation of the base flow (Fig. 8), further reflecting the global alteration of the boundary layer. To verify the experimentally observed spanwise shift of the CF vortices, a theoretical prediction of trajectory of the fundamental mode is calculated based on the previous LST results ($c_\mu = 1.65$) as follows:
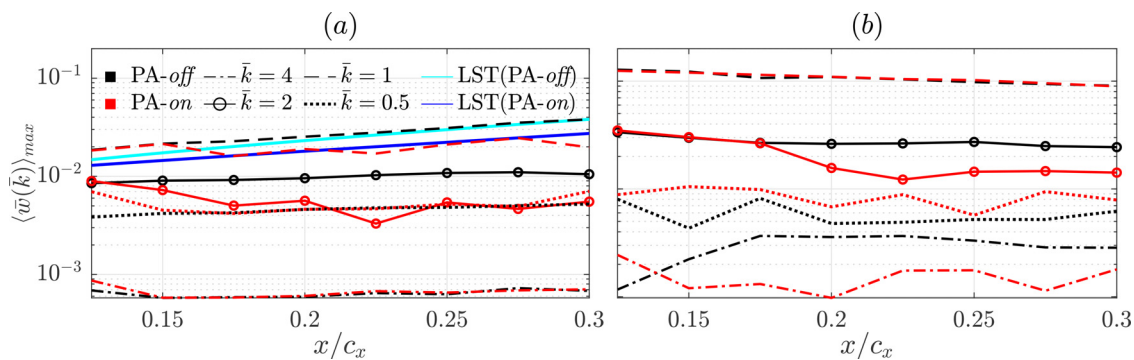

FIG. 11. Amplitudes of stationary Fourier modes for (a) DRE-*L*; (b) DRE-*H*. Data points are plotted from $x/c_x = 0.125$ to 0.3 with a step of 0.025. The wavenumber $\bar{k} = 0.25$, 0.5, 1, and 2 correspond to $\lambda = 16, 8, 4$, and 2 mm, respectively.

$$z = \int_0^x \tan\theta \, dx, \qquad (4)$$

where θ is the angle between the fundamental mode trajectory and the x axis. By convention, the angle θ is calculated as $\theta = \tan^{-1}(\beta_r/\alpha_r) + \pi/2$ in this work and illustrated in Fig. 12(a). Specifically, α_r is the real component of the complex streamwise wavenumber α, and β_r is the real spanwise wavenumber β.[40] As expected, θ is significantly altered at the PA forcing location (dashed line) while it collapses back to the non-forced values (PA-off) shortly downstream, demonstrating the localized effects of the PA forcing. In order to track the trajectory of the fundamental mode from the experimental data, the spanwise shift is calculated as $\bar{\varphi} \cdot \lambda_{DRE}$ at the location $\bar{y}_{max}$ where $\bar{\varphi} = \varphi/2\pi$ is the non-dimensional phase extracted from the spanwise FFT spectrum (Fig. 10). It should be noted that, the experimental spanwise shift $\bar{\varphi} \cdot \lambda_{DRE}$ is calculated in reference to the X axis and needs to be transformed to the x axis for comparison with LST results. The combined results are depicted in the xz plane and shown in Figs. 12(c) and 12(d). As expected, in the DRE-L case, the spanwise shift of the CF vortices is detected by LST, and the results show good agreement with the experimental measurements, though a small discrepancy is found downstream. Moreover, the vortex trajectory for PA-on appears to be parallel to the one of PA-off, due to the recovered angle θ downstream of the forcing area. Moreover, the vortex trajectories of DRE-H show a similarity to those of the DRE-L case. It appears that the modified trajectory of the stationary modes is independent from the local vortex amplitude and more likely to be determined by the modified boundary layer stability properties. Supplementary measurements at various PA forcing conditions (i.e., $12-15$ kV and $U_\infty = 22$ m/s) are implemented to further elucidate the effects of forcing strength on the spanwise shift of CF vortex trajectories. The non-dimensional FFT phase $\bar{\varphi}$ of the fundamental mode is calculated at $x/c_x = 0.275$, and the phase shift due to PA forcing is then estimated as $\Delta\bar{\varphi} = \bar{\varphi}_{on} - \bar{\varphi}_{off}$. As shown in Fig. 12(b), for both DRE cases, the phase shift of the fundamental modes monotonically increases with c_μ. It can be concluded that the BFM-based PA generates a significant modification on the boundary layer, which in turn can be reflected by the stationary CF vortex trajectories.

The CF vortex trajectory shift due to plasma forcing provides some interesting insight into the effects of BFM in relation to other control strategies. It can be proposed that the change in CF vortex trajectories can be further used to distinguish pure BFM effects in application cases of spanwise modulated or discrete PA. As mentioned before, discrete PAs (which are commonly used for the UFD strategy[24,43]) have been found to generate a combination of UFD and BFM effects under specific operating parameters (e.g., PA spacing, forcing amplitudes, and forcing direction). Based on the current results, it can be concluded that for applications of discrete PAs, the relative importance of BFM effects can be inferred by the change in CF vortex trajectories. Furthermore, the current outcome implies that the BFM strategy could be potentially beneficial to the direct attenuation strategy. Specifically, one of the application challenges for the direct attenuation strategy is the strict position accuracy with respect to the target stationary CF vortices. To resolve this problem, a BFM-based PA can be operated upstream of the control region to re-orient the target CF vortices (granted they are properly detected) to the desired locations by finely adjusting c_μ.

C. Effect on unsteady structures

Notwithstanding the identified sensitivity to DRE amplitudes, the general amplitude reduction of stationary CF instabilities and the trajectory alteration are attributed to the prime BFM mechanism, which reflects the overall boundary layer stabilization. Nonetheless, the PA forcing can also impose additional effects on the boundary layer. As mentioned earlier, realistic DBD forcing can inherently induce unsteady perturbations, which feature larger growth rates (than stationary CF modes). Figure 13 illustrates the standard deviation of temporal spanwise velocity fluctuations $\langle \bar{w}' \rangle$ for both DRE cases at $x/c_x = 0.225$. Evidently, unsteady fluctuations are considerably enhanced by the PA forcing, possibly resulting from quasi-stochastic processes in the PA micro-discharge, as suggested by Moralev et al.[29] As expected, due to the stronger stationary CF vortices (i.e., stronger shear stress modulation) for DRE-H, the PA-induced fluctuations are largely amplified and located in two distinct regions corresponding to the minimum and maximum $\partial\bar{w}/\partial\bar{z}$. In contrast, the unsteady
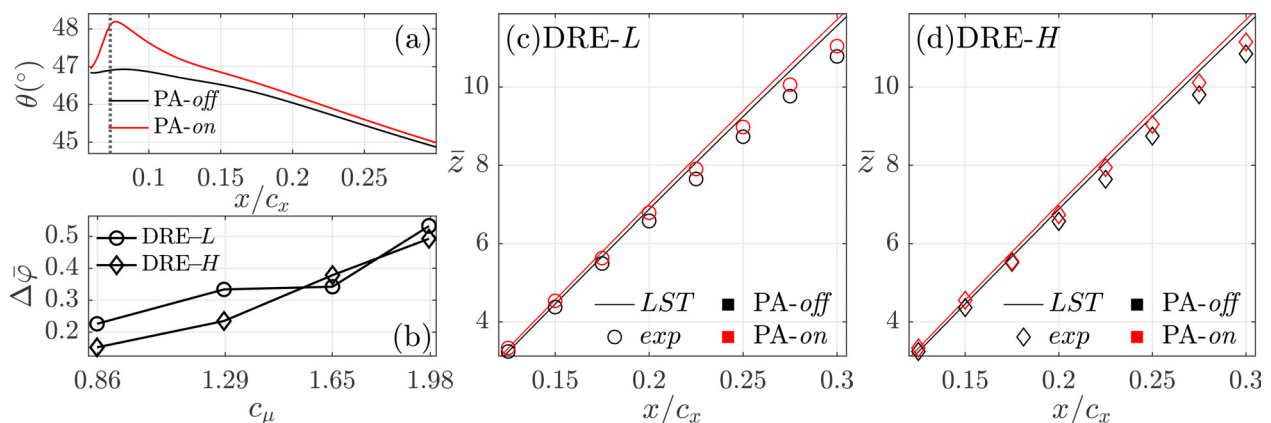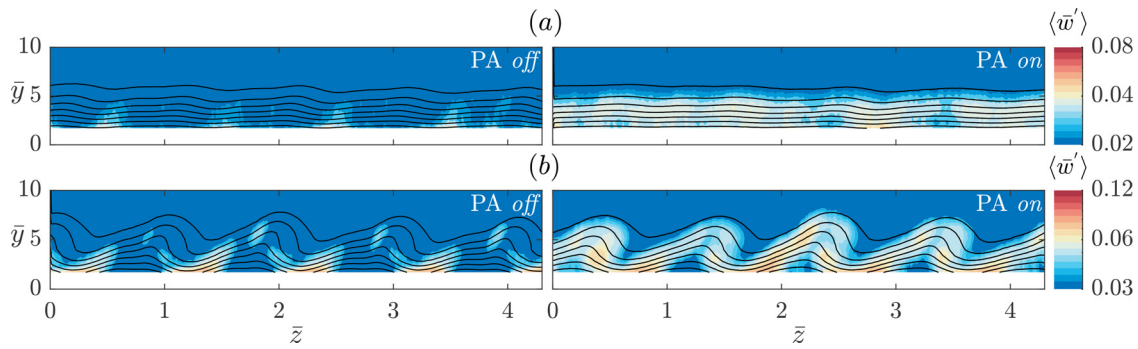

FIG. 12. (a) Wavenumber vector angle θ of the fundamental stationary mode calculated from LST. Vertical dashed line indicates the PA location; (b) experimentally determined relative phase shift of the fundamental mode vs momentum coefficient c_μ at $x/c_c = 0.275$; fundamental mode trajectories from experiment and LST for (c) DRE-L and (d) DRE-H.

FIG. 13. Standard deviation of temporal velocity fluctuations $\langle \bar{w}' \rangle$ for (a) DRE-*L*; (b) DRE-*H*. Plane location is at $x/c_x = 0.225$, and black iso-lines illustrate $\bar{w}$, ten levels from 0 to 0.9.

fluctuations for DRE-*L* are only mildly amplified without an evident spatial arrangement due to the relatively weak stationary vortices. Based on the predictions of LST calculations shown earlier, it is likely that part of these coherent structures is related to the development of naturally unstable modes such as type III, which essentially result from the interaction between stationary and traveling CF instabilities or secondary instabilities of type-I/II. However, these fluctuations cannot be conclusively segregated due to the absence of frequency information in the PIV measurements. As such, the fluctuation field will be further treated as a whole.

The amplitudes of the unsteady fluctuations are further evaluated as[44]

$$\bar{B} = \frac{1}{z_{max}} \frac{1}{\delta_{99}} \int_0^{z_{max}} \int_0^{\delta_{99}} \langle \bar{w}' \rangle ds, \tag{5}$$

where z_{max} is the spanwise extent of the measurement plane. The integral amplitudes $\bar{B}$ are collected in Fig. 14 along with the ratio $\bar{B}_{on}/\bar{B}_{off}$ (blue line). In contrast to the identified reduction of stationary CF instabilities due to the BFM effect, considerable unsteady disturbances are enhanced by the PA operation despite the remarkably reduced N factors for traveling CF modes predicted by LST. Compared with DRE-*L*, the fluctuation amplitudes are evidently higher in the DRE-*H* case though the ratio $\bar{B}_{on}/\bar{B}_{off}$ maintains the same level for both DREs.

The considerable unsteady fluctuations observed in this section reconcile with the work of Downs and White.[44] In their highest T_u case, stationary CF modes are found to be weakened through nonlinear interaction with traveling CF instabilities of sufficient amplitudes. Though the current experiment was conducted in different

wind tunnel conditions (i.e., low T_u), there still remains the possibility that PA-induced fluctuations contribute to the reduction of stationary CF modes, as observed in Sec. IV A. Nonetheless, this assumption cannot be confirmed in the present paper. For the future work to validate this assumption, the DRE array needs to be placed downstream of the PA to eliminate the BFM effects.

Nonetheless, it can be concluded that the PA forcing essentially imposes two (potentially competing) effects in the boundary layer. One is generally reducing stationary CF instabilities, and the other is enhancing unsteady fluctuations.

V. CONCLUDING REMARKS

In this paper, a DBD plasma actuator, which is specially configured to enable base flow modification (BFM), is used to control CF instabilities in a swept wing boundary layer. To realize the BFM strategy, a 2D spanwise-invariant PA is constructed and positioned close to the leading edge ($x/c_x = 0.073$). The actuator is oriented to produce a volume-distributed body force normal to the leading edge in a direction against the incoming flow. The base flow modification is investigated under various PA momentum coefficients c_μ. Consistent with the recent evidence of Serpieri *et al.*[27] and Yadala *et al.*[30] as well as the working BFM hypothesis, the CF component is experimentally proven for the first time to be reduced by the BFM-based PA forcing. As expected, higher c_μ leads to a more effective reduction of the CF component. In addition, it is found that the BFM strategy is more effective in manipulating the CF component w_s, even though the added momentum is delivered in the bulk velocity u_s direction. As a result, the dissimilar reduction between u_s and w_s leads to a directional alteration of the base flow. The flow direction is found significantly affected
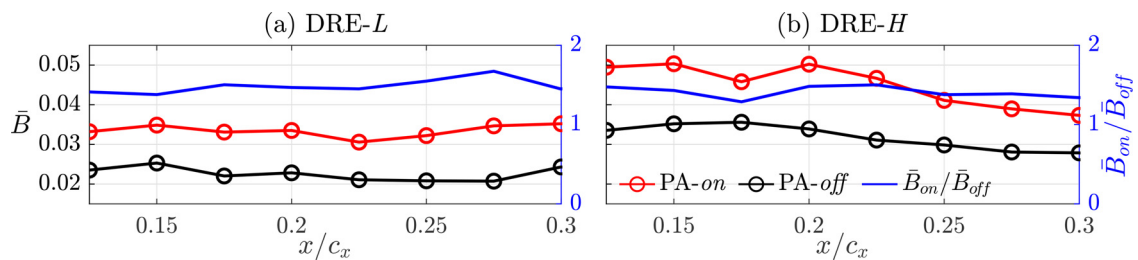
FIG. 14. Integral amplitudes of unsteady disturbances for (a) DRE-*L*; (b) DRE-*H*. The blue line illustrates the ratio $\bar{B}_{on}/\bar{B}_{off}$ and refers to the right *y* axis.

near the wall while remaining unchanged in the freestream, showing a strong near-wall influence of PA forcing.

PA effects on both stationary CF instabilities and unsteady disturbances are investigated by planar-PIV. Two DRE arrays featuring different height h_{DRE} are placed near the leading edge, thus conditioning linear and non-linear growth of stationary CF vortices, respectively. Both DRE cases demonstrate that the super-harmonic modes are significantly reduced due to BFM, while the fundamental mode reduction is only found in the low-amplitude DRE case. The disparity of the BFM effects in reducing the fundamental modes appears to be attributed to h_{DRE} and, in turn, the amplitudes of the stationary CF vortices in the region interact with the plasma body force. At least in the linear growth DRE case, the general amplitude reduction of stationary CF instabilities agrees with the LST results, demonstrating the BFM effect due to the PA forcing.

A particular effect identified in the present study is a notable spanwise shift of the stationary CF vortex trajectories due to PA forcing. The effect is experimentally observed as well as predicted by LST. The modification of the trajectory is found to originate from the change of local boundary layer stability in the plasma region. While this shift is expected to be largely irrelevant to the effectiveness of BFM as a transition delay technique, the ability of the PA forcing to shift CF vortices might be leveraged in other flow control techniques in which the spatial phase of the instabilities is important (e.g., the localized suction technique[45] and the PA-based direct attenuation strategy[23]).

Finally, in contrast to the reduced stationary CF instabilities, unsteady velocity fluctuations are found to be intensively amplified by the PA forcing in both DRE amplitude cases. These enhanced unsteady disturbances can possibly contribute to the reduction of stationary CF instabilities. On the other hand, their significant growth rates can destabilize the boundary layer, thus weakening the BFM net effect. These competing effects emerge as a key point and challenge in need of further investigation toward improving the BFM performance.

AUTHOR DECLARATIONS
Conflict of Interest

The authors have no conflicts to disclose.

Author Contributions

Kaisheng Peng: Conceptualization (lead); Data curation (lead); Formal analysis (lead); Investigation (equal); Methodology (lead); Supervision (equal); Writing – original draft (lead); Writing – review & editing (equal). **Joerie Arkesteijn:** Data curation (equal); Formal analysis (equal); Methodology (equal). **Francesco Avallone:** Writing – review & editing (equal). **Marios Kotsonis:** Methodology (equal); Supervision (equal); Writing – review & editing (lead).

DATA AVAILABILITY

The data that support the findings of this study are available from the corresponding author upon reasonable request.

REFERENCES

[1] W. S. Saric, H. L. Reed, and E. B. White, "Stability and transition of three-dimensional boundary layers," Annu. Rev. Fluid Mech. **35**, 413–440 (2003).

[2] H. Bippes, "Basic experiments on transition in three-dimensional boundary layers dominated by crossflow instability," Prog. Aerosp. Sci. **35**, 363–412 (1999).

[3] M. R. Malik, F. Li, M. M. Choudhari, and C.-L. Chang, "Secondary instability of crossflow vortices and swept-wing boundary-layer transition," J. Fluid Mech. **399**, 85–115 (1999).

[4] R. D. Joslin, "Aircraft laminar flow control," Annu. Rev. Fluid Mech. **30**, 1–29 (1998).

[5] K. Krishnan, O. Bertram, and O. Seibel, "Review of hybrid laminar flow control systems," Prog. Aerosp. Sci. **93**, 24–52 (2017).

[6] R. Messing and M. J. Kloker, "Investigation of suction for laminar flow control of three-dimensional boundary layers," J. Fluid Mech. **658**, 117 (2010).

[7] W. Saric, R. Carrillo, Jr., and M. Reibert, "Leading-edge roughness as a transition control mechanism," AIAA Paper No. 1998-781, 1998.

[8] P. Wassermann and M. Kloker, "Mechanisms and passive control of crossflow-vortex-induced transition in a three-dimensional boundary layer," J. Fluid Mech. **456**, 49 (2002).

[9] S. M. Hosseini, D. Tempelmann, A. Hanifi, and D. S. Henningson, "Stabilization of a swept-wing boundary layer by distributed roughness elements," J. Fluid Mech. **718**, R1 (2013).

[10] W. S. Saric, D. E. West, M. W. Tufts, and H. L. Reed, "Experiments on discrete roughness element technology for swept-wing laminar flow control," AIAA J. **57**, 641–654 (2019).

[11] Z. Guo and M. J. Kloker, "Effects of low-frequency noise in crossflow transition control," AIAA J. **58**, 1068–1078 (2020).

[12] C. Enloe, T. E. McLaughlin, R. D. VanDyken, K. Kachner, E. J. Jumper, and T. C. Corke, "Mechanisms and responses of a single dielectric barrier plasma actuator: Plasma morphology," AIAA J. **42**, 589–594 (2004).

[13] M. Kotsonis, "Diagnostics for characterisation of plasma actuators," Meas. Sci. Technol. **26**, 092001 (2015).

[14] T. C. Corke, C. L. Enloe, and S. P. Wilkinson, "Dielectric barrier discharge plasma actuators for flow control," Annu. Rev. Fluid Mech. **42**, 505–529 (2010).

[15] N. Benard and E. Moreau, "Electrical and mechanical characteristics of surface ac dielectric barrier discharge plasma actuators applied to airflow control," Exp. Fluids **55**, 1846 (2014).

[16] S. Grundmann and C. Tropea, "Experimental transition delay using glow-discharge plasma actuators," Exp. fluids **42**, 653–657 (2007).

[17] M. Kotsonis, R. Giepman, S. Hulshoff, and L. Veldhuis, "Numerical study of the control of Tollmien–Schlichting waves using plasma actuators," AIAA J. **51**, 2353–2364 (2013).

[18] P. C. Dörr and M. J. Kloker, "Numerical investigations on Tollmien–Schlichting wave attenuation using plasma-actuator vortex generators," AIAA J. **56**, 1305–1309 (2018).

[19] Z. Guo and M. J. Kloker, "Control of crossflow-vortex-induced transition by unsteady control vortices," J. Fluid Mech. **871**, 427–449 (2019).

[20] P. Dörr and M. Kloker, "Stabilisation of a three-dimensional boundary layer by base-flow manipulation using plasma actuators," J. Phys. D **48**, 285205 (2015).

[21] P. C. Dörr and M. J. Kloker, "Crossflow transition control by upstream flow deformation using plasma actuators," J. Appl. Phys. **121**, 063303 (2017).

[22] N. Shahriari, M. R. Kollert, and A. Hanifi, "Control of a swept-wing boundary layer using ring-type plasma actuators," J. Fluid Mech. **844**, 36–60 (2018).

[23] P. Dörr and M. Kloker, "Transition control in a three-dimensional boundary layer by direct attenuation of nonlinear crossflow vortices using plasma actuators," Int. J. Heat Fluid Flow **61**, 449–465 (2016).

[24]Z. Wang, L. Wang, and S. Fu, "Control of stationary crossflow modes in swept Hiemenz flows with dielectric barrier discharge plasma actuators," Phys. Fluids **29**, 094105 (2017).

[25]S. Yadala, M. T. Hehner, J. Serpieri, N. Benard, and M. Kotsonis, "Plasma-based forcing strategies for control of crossflow instabilities," AIAA J. **59**(9), 3406–3416 (2021).

[26]C. Y. Schuele, T. C. Corke, and E. Matlis, "Control of stationary cross-flow modes in a Mach 3.5 boundary layer using patterned passive and active roughness," J. Fluid Mech. **718**, 5–38 (2013).

[27]J. Serpieri, S. Y. Venkata, and M. Kotsonis, "Conditioning of cross-flow instability modes using dielectric barrier discharge plasma actuators," J. Fluid Mech. **833**, 164–205 (2017).

[28]S. Yadala Venkata, M. Hehner, J. Serpieri, N. Benard, and M. Kotsonis, "Swept-wing transition control using AC-DBD plasma actuators," AIAA Paper No. 2018-3215, 2018.

[29]I. Moralev, I. Selivonin, and M. Ustinov, "On the stochastic forcing of the boundary layer by plasma actuators," Exp. Fluids **60**, 177 (2019).

[30]S. Yadala, M. T. Hehner, J. Serpieri, N. Benard, P. C. Dörr, M. J. Kloker, and M. Kotsonis, "Experimental control of swept-wing transition through base-flow modification by plasma actuators," J. Fluid Mech. **844**, R2 (2018).

[31]S. A. Baranov, S. L. Chernyshev, V. Y. Khomich, A. P. Kiselev, A. P. Kuryachii, S. I. Moshkunov, I. E. Rebrov, D. S. Sboev, S. N. Tolkachev, and V. A. Yamshchikov, "Experimental cross-flow control in a 3D boundary layer by multi-discharge plasma actuators," Aerosp. Sci. Technol. **112**, 106643 (2021).

[32]R. Merino-Martínez, A. R. Carpio, L. T. L. Pereira, S. van Herk, F. Avallone, D. Ragni, and M. Kotsonis, "Aeroacoustic design and characterization of the 3D-printed, open-jet, anechoic wind tunnel of delft university of technology," Appl. Acoust. **170**, 107504 (2020).

[33]J. Serpieri and M. Kotsonis, "Design of a swept wing wind tunnel model for study of cross-flow instability," AIAA Paper No. 2015-2576, 2015.

[34]K. Peng and M. Kotsonis, "Cross-flow instabilities under plasma actuation: Design, commissioning and preliminary results of a new experimental facility," in AIAA Scitech 2021 Forum (AIAA, 2021), p. 1194.

[35]A. Sciacchitano and B. Wieneke, "PIV uncertainty propagation," Meas. Sci. Technol. **27**, 084006 (2016).

[36]J. Arkesteijn, "Cross-flow instability control through base-flow modification using AC-DBD plasma actuators: An experimental investigation," Master thesis (Delft University of Technology, 2021).

[37]M. Kotsonis, S. Ghaemi, L. Veldhuis, and F. Scarano, "Measurement of the body force field of plasma actuators," J. Phys. D **44**, 045204 (2011).

[38]R. Pereira, D. Ragni, and M. Kotsonis, "Effect of external flow velocity on momentum transfer of dielectric barrier discharge plasma actuators," J. Appl. Phys. **116**, 103301 (2014).

[39]G. Zoppini, S. Westerbeek, D. Ragni, and M. Kotsonis, "Receptivity of cross-flow instability to discrete roughness amplitude and location," J. Fluid Mech. **939**, A33 (2022).

[40]L. M. Mack, "Boundary-layer linear stability theory," Technical Report No. 709 (California Institute of Technology Pasadena, Jet Propulsion Lab, 1984).

[41]A. F. Rius-Vidales and M. Kotsonis, "Influence of a forward-facing step surface irregularity on swept wing transition," AIAA J. **58**, 5243–5253 (2020).

[42]M. Malik, F. Li, and C.-L. Chang, "Crossflow disturbances in three-dimensional boundary layers: Nonlinear development, wave interaction and secondary instability," J. Fluid Mech. **268**, 1–36 (1994).

[43]P. Dörr, M. Kloker, and A. Hanifi, "Effect of upstream flow deformation using plasma actuators on crossflow transition induced by unsteady vortical free-stream disturbances," AIAA Paper No. 2017-3114, 2017.

[44]R. S. Downs and E. B. White, "Free-stream turbulence and the development of cross-flow disturbances," J. Fluid Mech. **735**, 347 (2013).

[45]T. Friederich and M. J. Kloker, "Control of the secondary cross-flow instability using localized suction," J. Fluid Mech. **706**, 470–495 (2012).